Wind and Structures, *Vol. 27, No. 6 (2018) 381-397*
DOI: https://doi.org/10.12989/was.2018.27.6.381

Nonlinear fluid-structure interaction of bridge deck: CFD analysis and semi-analytical modeling

Christian Grinderslev[1], Mikkel Lubek[2] and Zili Zhang*[3]

[1]*Department of Wind Energy, Technical University of Denmark (Risø Campus), 4000 Roskilde, Denmark*
[2]*COWI, 8000 Aarhus, Denmark*
[3]*Department of Engineering, Aarhus University, 8000 Aarhus, Denmark*

(Received February 3, 2018, Revised June 30, 2018, Accepted July 28, 2018)

Abstract. Nonlinear behavior in fluid-structure interaction (FSI) of bridge decks becomes increasingly significant for modern bridges with increasing spans, larger flexibility and new aerodynamic deck configurations. Better understanding of the nonlinear aeroelasticity of bridge decks and further development of reduced-order nonlinear models for the aeroelastic forces become necessary. In this paper, the amplitude-dependent and neutral angle dependent nonlinearities of the motion-induced loads are further highlighted by series of computational fluid dynamics (CFD) simulations. An effort has been made to investigate a semi-analytical time-domain model of the nonlinear motion induced loads on the deck, which enables nonlinear time domain simulations of the aeroelastic responses of the bridge deck. First, the computational schemes used here are validated through theoretically well-known cases. Then, static aerodynamic coefficients of the Great Belt East Bridge (GBEB) cross section are evaluated at various angles of attack, leading to the so-called nonlinear backbone curves. Flutter derivatives of the bridge are identified by CFD simulations using forced harmonic motion of the cross-section with various frequencies. By varying the amplitude of the forced motion, it is observed that the identified flutter derivatives are amplitude-dependent, especially for A_2^* and H_2^* parameters. Another nonlinear feature is observed from the change of hysteresis loop (between angle of attack and lift/moment) when the neutral angles of the cross-section are changed. Based on the CFD results, a semi-analytical time-domain model for describing the nonlinear motion-induced loads is proposed and calibrated. This model is based on accounting for the delay effect with respect to the nonlinear backbone curve and is established in the state-space form. Reasonable agreement between the results from the semi-analytical model and CFD demonstrates the potential application of the proposed model for nonlinear aeroelastic analysis of bridge decks.

Keywords: computational fluid dynamics; flutter derivatives; nonlinear aeroelasticity; nonlinear semi-analytical model

1. Introduction

When designing highly slender structures such as long span bridges, fluid-structure interaction (FSI) is of high importance, as it can potentially lead to large amplitude vibrations or even aeroelastic instability, such as classical flutter. The prediction of flutter instability is of major concern in the design of long span bridges. Right now, the flutter stability analysis of suspension bridges is mostly based on the semi-empirical model defined by Scanlan (Scanlan 1978, Simiu and Scanlan 1996), using the so-called flutter derivatives for calculating the aeroelastic loads. Due to the bluff nature of the deck, sectional model tests in wind tunnels need to be performed to determine the deck-specific flutter derivatives (Starossek *et al*. 2009).

Essentially, the flutter derivatives represent the frequency response functions (FRFs) for the aeroelastic loads due to forced harmonic motions of the bridge deck. Therefore, although this semi-empirical model is able to handle unsteadiness of the aeroelastic loads that are functions of frequency, it is a linear model. In reality, the flow-deck system is an inherently nonlinear system, due to the flow separation and reattachment around the deck with sharp edges and railings, making this widely-used linear unsteady model questionable. The nonlinear behavior of the aeroelastic loads on the deck is seen in various ways (Wu and Kareem 2013a), such as the non-proportional relations between input and output, multiple frequencies excited by a single frequency, and amplitude dependency of the aeroelastic behavior. The most straightforward nonlinear model for aerodynamic/aeroelastic loads is based on the quasi-steady (QS) theory (Kovacs *et al*. 1992), which describes the aerodynamic/aeroelastic loads through a static nonlinear relationship between the incident flow and the flow-induced forces on the structure. However, it cannot take into consideration the unsteady features in FSI with fluid memory effects. In order to improve this model, a corrected QS theory-based model has been proposed where a modified coefficient is introduced to partly account for fluid memory effects (Diana *et al.* 1993), although the proper calibration of the coefficient is challenging. Later, a hybrid model was proposed (Chen *et al*. 2000, Chen and Kareem 2003), which has a clear connection with the Scanlan's semi-empirical linear model. The QS theory-based nonlinear model is used when the reduced wind velocity is relatively high (the low-frequency part) while the semi-empirical linear model is utilized for the high-

*Corresponding author, Assistant Professor
E-mail: zili_zhang@eng.au.dk

http://www.techno-press.com/journals/was&subpage=7
ISSN: 1226-6116 (Print), 1598-6225 (Online)

frequency part. The difficulty lies in determining the cut-off frequency dividing the turbulence and structural response into low-frequency and high-frequency parts. From a point of view of nonlinear hysteresis loops relating aerodynamic force with the instantaneous angle of attack, a rheological model was proposed using the aerodynamics-mechanics analogy (Diana *et al*. 2008, 2010). Parameters of the rheological model need to be identified from sectional model tests in wind tunnels. More recently, a Volterra theory based nonlinear analysis framework has been proposed for bluff-body aerodynamics (Wu and Kareem, 2013a, 2015). In this model, the linear convolution scheme (time domain equivalence of the flutter derivatives) is logically extended to the summation of linear and nonlinear convolution schemes, and a generalized impulse function-based scheme is used for identification of the Volterra kernels.

Traditionally, procedures based on wind tunnel tests have been dominantly used for investigating FSI and aeroelastic loads of bridge decks, and for identifying parameters needed in the linear/nonlinear aeroelastic load models. Recently, the advances in computational power and turbulence modeling enables computational fluid dynamics (CFD), the numerical representation of wind tunnel tests, an attractive alternative for investigating aeroelasticity and aerodynamics of bridge decks (Liaw 2005, Stærdahl *et al.* 2007, Brusiani *et al.* 2013, Nieto *et al*. 2010). Some uncertainties are still present in the CFD simulation results due to the fully turbulent, unsteady, three-dimensional flow conditions around the bluff body, but well-chosen turbulence models and fine discretization of the computational domain have shown to lead to good results. The advantage of CFD is its flexibility in the modelling of the FSI problem.

Although the subject of nonlinear aeroelastic modeling of bridge decks has already been tackled in literature multiple times as summarized above, there is still need for further investigations on developing reduced-order models that incorporate both the physical insight of the nonlinear motion-induced loads and the computational efficiency. The aerodynamic mechanics analogy of the rheological model (Diana *et al*. 2008, 2010) is very novel and interesting, but a large number of coefficients need to be calibrated through system identification technique. The Volterra theory based nonlinear model (Wu and Kareem 2013a, 2015), on the other hand, might be relatively computationally expensive because linear and nonlinear convolution integrals need to be solved in the time domain. Therefore, the goal of the present paper is to get a deeper understanding of nonlinear behavior of motion-induced loads through CFD simulations, and to develop a nonlinear time-domain model that is based on physical insight of the nonlinear flow-deck system and that can be incorporated into equations of motion of the bridge deck. To do so, an effort has been made to establish a dynamic-stall type model in terms of the state-space formulation, which can be efficiently solved in the time-domain.

In the present paper, extensive CFD simulations have been carried out to investigate nonlinear aeroelasticity of the deck section of the Great Belt East Bridge (GBEB).

Unsteady Reynolds-averaged Navier-Stokes (uRANS) model with SST k−ω turbulence model, which is characterized a good compromise between accuracy and computational cost, is utilized in the present study. The computational schemes used here are first validated by experimentally or theoretically well-known cases, i.e., flow around stationary cylinders (circular and square), and an oscillating flat plate with Theodorsen’s solution (Fung 2002). Next, static aerodynamic coefficients of the GBEB cross-section are evaluated at various angles of attack, resulting in the nonlinear back-bone curves. Flutter derivatives are then identified by CFD simulations using forced harmonic translational and rotational motions of the cross-section with various reduced frequencies. The resultant predictions are compared with experimental and other numerical results. By varying the amplitude of the forced motion, it is observed that the identified flutter derivatives are amplitude-dependent, especially for the A_2^* and H_2^* parameters. Further, forced harmonic motions around different neutral angles have been performed, and the corresponding hysteresis loops relating the angle of attack and the motion-induced lift/moment are investigated. The nonlinear behavior is clearly observed from the significant difference in the hysteresis loops. Based on the steady and unsteady CFD results, a semi-analytical model for describing the nonlinear motion-induced lift and moment on the bridge deck is proposed, which is based on combining the nonlinear back-bone curve with the modelled memory delay effects of the unsteady flow. Reasonable agreement has been obtained between the results from the model and from CFD simulations.

2. Computational scheme and its validation

All CFD simulations have been conducted using the commercial software STAR-CCM+, where thin 3D section simulations have been made to capture the three-dimensional vortices created at separation. An implicit unsteady solver based on the transient SIMPLE scheme with Rhie-and-Chow-type pressure-velocity coupling and a second order accurate upwind convective scheme is used for all simulations. uRANS approach coupled with SST *k-ω* turbulence model (Menter *et al.* 2003) is used, as it is considered as the best compromise between accuracy and computational cost (Brusiani *et al.* 2013), also because large amount of simulations is to be carried out for parametric study in the present paper. The SST *k-ω* turbulence model consists of a blending between the k-ε model (which does not allow the direct integration through the wall boundary layer, but is less sensitive to inlet turbulence boundary conditions) and *k-ω* model (which allows the direct integration through the wall boundary layer, but is highly sensitive to inlet turbulence boundary conditions). The weighting between these two is controlled by the wall distance. The SST *k-ω* turbulence model preserves all the main advantages of the classical *k-ω* model, but it has been proved to be less sensitive to inlet conditions. One reason uRANS in this specific case is expected sufficiently accurate, is the well-defined separation points at the edges of the bridge deck. For more streamlined cross-sections the necessity of more complex turbulence modelling like large eddy simulations (LES) arises, as the separation point locations can be of high importance. The use of uRANS method for bridge aerodynamics is well validated in (Brusiani *et al*. 2013, Tang *et al*. 2017 and Mannini *et al*. 2016). An extensive review about using RANS SST for flutter analysis can be found in (Patruno 2015), where different bridge deck sections are studied using both experiments and RANS. The comparison concludes that in general, RANS predicts accurate results for flutter onset. However, cautions need to be taken for decks with secondary elements, and decks at high stall. This is the case for the current study, thus experimental validation is of high importance.

Moreover, instead of using a fine mesh throughout the computational domain, different refinements have been used at different regions. The mesh around the solid is refined with a prism layer, a surface layer and a wake refinement, while a coarser mesh (polyhedral cells) is used in the remaining domain.

In order to validate the computational scheme and analysis parameters, benchmark test cases are studied, i.e., flow around stationary cylinders with two geometrically simple cross section shapes (circular and rectangular) where experimental results are available, and a harmonically oscillating flat plate in a uniform flow around zero angle of attack where analytic solutions are available.

2.1 Validation with stationary cylinders

As shown in Fig. 1, a stationary circular cylinder and a square cylinder with a diameter/side dimension of D = 0.1m are placed into a fluid flow 3D domain, undergoing various Reynolds numbers obtained by changing the flow velocity. The domain sizes (width × height × depth) for the circular and rectangular cylinders are (24D × 16D × 2D) and (32D × 16D × 2D), respectively. The boundary conditions are velocity inlet and pressure outlet for the left and right side on Fig. 1, respectively, and symmetry planes on all other domain sides. The object surface is modelled as no slip wall. The domain is discretized with polyhedral cells, growing in size away from the cylinder with a growth rate of 1.1. The cells around the cylinder are modelled as prism layers with a maximum size of 8.17·10−4 m, and fine custom refinement is made on the surface of the bodies. To capture the wake behind the cylinder, a wake refinement has been used with a growth rate of 1.3.

Both the circular and square cylinder cases are well documented experimentally by e.g., (Sumer and Fredsøe 1997, Lysenko *et al*. 2012, Demartino, 2017, Dutta *et al*. 2008, Saha e*t al*. 2003), for various values of Reynolds numbers. The results of the CFD simulations are compared with the experimental results, in terms of drag coefficient C_D, lift coefficient C_L, and vortex shedding period T_s, as shown in Table 1.

As seen, good agreement is found between the CFD and the experimental results. Furthermore, the flow patterns for the three different Reynolds numbers (Re) behave similarly as what the experiments have shown. Fig. 2(a) shows the flow pattern around the circular cylinder for Re=3900 corresponding to the sub-critical regime, where regular shedding of vortices from the two sides of the cylinder occur forming a Karman vortex street.

Table 1 Results of the CFD-simulations for the circular cylinders compared with the experimental results

Re [−]	C_D [-]	Exp. C_D	C_L [-]	Exp. C_L	T_s [-]	Exp. T_s
Circular						
1	64.69	$4-\infty$	0.0002	0	-	-
3900	1.20	0.84-1.3	−0.0008	0	1.280	1.282
500,000	0.28	0.3-0.5	−0.0126	0	-	-
Square						
100	1.48	1.50-2.00	0.001	0	-	-
400	1.74	1.47-2.20	−0.091	0	17.67	18.52
10,000	2.12	2.00	−0.007	0	0.769	-

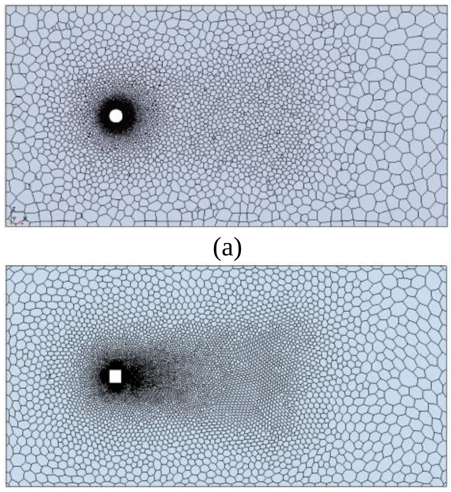

(a)

(b)

Fig. 1 The computational domain and mesh for the stationary cylinders: (a) Circular and (b) Square

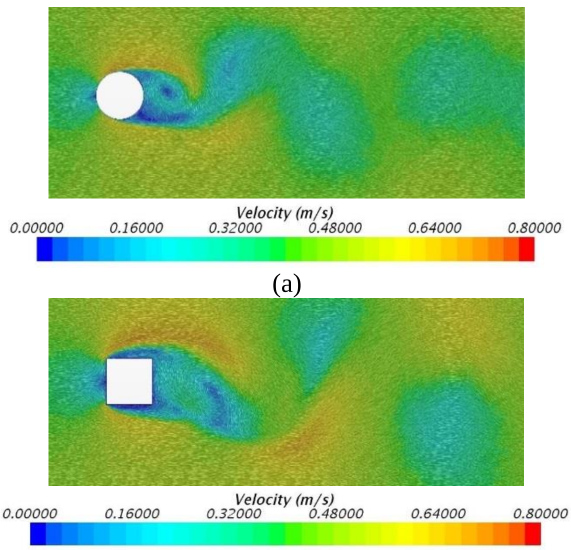

(a)

(b)

Fig. 2 Velocity field for the stationary cylinders. (a)Circular, Re=3900, (b) Square and Re=400

2.2 Validation with oscillating flat plate

3D CFD simulations on a harmonically oscillating flat plate (theoretically zero thickness) in a uniform flow is performed as a benchmark test case, in order to gain confidence of dynamic mesh for investigating the aeroelastic loads due to the forced motion of the body. The harmonically oscillating flat plate as shown in Fig. 3 with fully-attached flow is analytically well defined in classical aeroelasticity theory by Theodorsen (Fung 2002). The lift on the plate can be calculated using the Theodorsen circulation function C(k), where $k=\frac{\omega b}{U}$ is the reduced frequency with ω the angular frequency (Fung 2002)

$$L(t) = 2\pi b\rho U^2\, C(k)\left(\alpha_0+\frac{i}{b}kh_0+\frac{1}{2}\; i\; k\; \alpha_0\right)e^{ik\tau} + \left(-\rho\pi U^2k^2h_0+\rho\pi bU^2 i\; k\; \alpha_0\right)e^{ik\tau} \tag{1}$$

where b is half the plate width, ρ the fluid density, U the flow velocity, α_0 the torsional motion amplitude and h_0 the translation amplitude of the forced harmonic motions.

A thin 3D strip of the flat plate with a depth of 20% of the width is modelled. In this study, the overset mesh function of STAR-CCM+ is used. As shown in Fig. 4, a general mesh is made for the fluid domain, which is used as the background mesh. In the region around the plate, another mesh is made which follows the movement of the plate. The overset mesh separates the overlapping part of the two regions and information is transferred between the domain mesh to the mesh within the plate area. In the intersection between the two regions, the mesh is updated for each step. The motion is applied to the entire plate region, and for each time step, the mesh in the interface is recalculated to connect the in- and outside mesh. Similar as the stationary cylinder cases, mesh refinement has been made near the walls and in the near wake.
Two harmonic motion cases have been investigated, namely vertical translation and rotation around the center. The amplitudes for translation and rotation are set to be h_0 = $0.003m/s$ and $\alpha_0 = 3°$, respectively. The angular frequency for both motions are chosen to be $\omega = 10\pi\ rad/s$.
The simulations have been performed with an implicit unsteady solver, with a time step of 0.001s. The lift coefficient $C_L(t)=\frac{L(t)}{1/2\rho U^2 A_{ref}}$ has been monitored for both cases, and the time series are compared with analytical results as shown in Fig. 5. It is seen that for both translation and rotation motions, the motion-induced lift force is in full agreement with the analytical results, in terms of both the phases and amplitudes. Table 2 shows the comparison of the amplitudes identified from the CFD simulation and that calculated by Theodorsen solution.

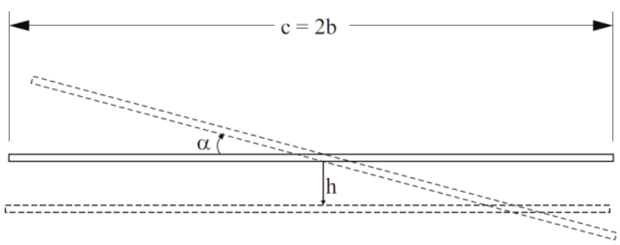

Fig. 3 Flat plate notations

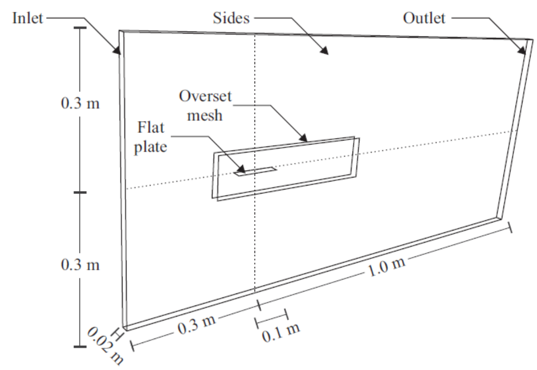

(a)

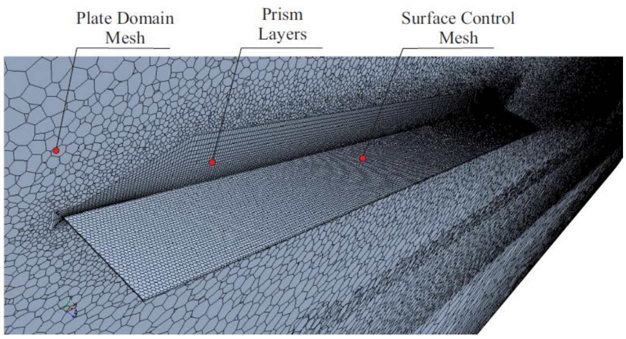

(b)

Fig. 4 Computational 3D model of the flat plate. (a) Computational domain around flat plate and (b) Mesh refinement around flat plate

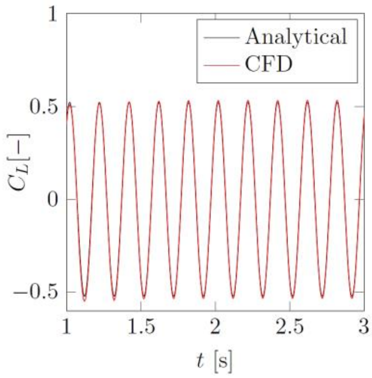

(a)

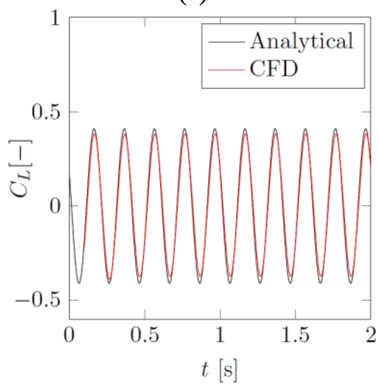

(b)

Fig. 5 Comparison of the motion-induced lift $C_L(t)$. (a) Translation $h(t)$ as the input, (b) Rotation $\alpha(t)$ as the input

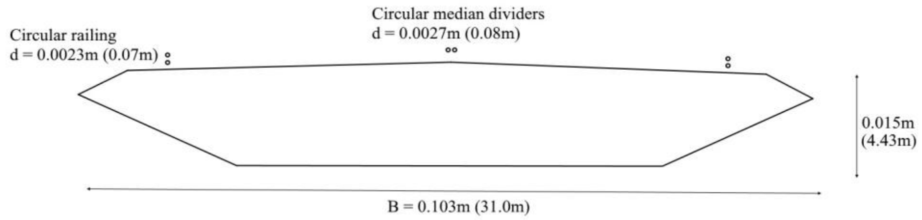

Fig. 6 Modelled scaled geometry. Full scale dimensions in parenthesis

Table 2 Comparison of the amplitudes of $C_L(t)$ between analytical solution and CFD simulations

Case	Analytical	CFD	Relative Error
Translation *h(t)*	0.522	0.533	2.16%
Rotation *α(t)*	0.410	0.384	-6.43%

3. Great Belt East Bridge analysis

The Great Belt East Bridge (GBEB) is a long-spanned suspension bridge in Denmark, which has undergone much research before and after construction. In the present study, experimental results from Danish Maritime Institute (DMI) (Reinholdt *et al.* 1992) and University of Western Ontario (UWO) (Davenport *et al*. 1992) are used for validation of the CFD simulation results. Note that UWO (Davenport *et al*. 1992) do not state the specific section type tested, but only the general section dimensions, which are the same for the two experiments. The bridge deck has been modelled in STAR-CCM+ in a same scale as in the wind tunnel tests carried out at UWO (1:300), including horizontal railing and median dividers as shown in Fig. 6.

Both stationary and dynamic scenarios are investigated. During the stationary scenario, the static aerodynamic forces acting on the fixed bridge deck cross-section are evaluated at various angles of attack, leading to the nonlinear backbone curves. During the dynamic scenario, vertical and rotational forced harmonic motions (with different frequencies) are separately imposed to the cross-section rotational center. The resulting unsteady self-induced aerodynamic forces are identified in terms of the flutter derivatives.

3.1 Modelling procedure

With the validated results from the aforementioned benchmark case studies, the procedure for simulating the flow around the bridge deck is similar, however with much higher degree of refinement. The railing and the median dividers are modelled, but guide vanes, cables and vertical components are omitted (Bruno and Mancini 2002).

In order to choose the appropriate domain size along with refinement degree, sensitivity analyses were conducted. In previous studies by e.g., (Tang *et al.* 2017, Mannini *et al*. 2016 and Stærdahl *et al*. 2007) good results have been found using 2D simulations.

In the sensitivity analyses of the present study however, significant differences are found between monitored forces using 2D and 3D approaches. For this reason, it was chosen to use 3D for all simulations. The reason for the monitored 3D effects might be the included railing, as this is a significant difference from the previous 2D studies mentioned.

The domain size is finally chosen as a length of *13B*, a height of *4.3B* and a depth of *0.06B*, where *B* is the down scaled deck width. As with the flat plate, a thin slice of the deck is modelled with the depth of the domain. The deck is scaled 1:300 to resemble the model of the validation experiment at UWO. It is placed at the 1/3 point of the domain length, as shown in Fig. 7(a).

As shown in Fig. 7(b), the mesh is configured by refining areas of high gradient pressure, which leads to high refinement around edges and surfaces. Polyhedral cells have been used, and for the dynamic cases the overset mesh interface is chosen around the interior region containing the deck. The overset mesh method has become popular for moving structures in CFD, because of its robustness and only few cells need updates per timestep. An alternative method could be the mesh deformation method as adopted in (Guo *et al*. 2017) for a similar bridge deck study.

In the present paper, it is found from mesh sensitivity studies that the simulation results are more mesh-sensitive for the stationary cases, and hence two mesh configurations are chosen. For the stationary and dynamic cases, 6.7 million cells and 3.2 million cells have been used, respectively.

The simulated flow is modelled as uniform and implicit unsteady with SST *k-ω* turbulence, and incompressibility is assumed. The time step for stationary and dynamic cases are set to be 0.01 sec and 0.002 sec, respectively.

3.2 Stationary analysis

For the stationary cases simulated, 9 different angles of attack have been evaluated in the range between ±15°. For each case, the aerodynamic force coefficients have been monitored, together with the pressure distribution around the deck and the flow features.

Using the mean values of the aerodynamic force coefficients, the backbone curves have been generated as a function of angle of attack and validated with experimental results from DMI (Reinholdt *et al*. 1992) and UWO (Davenport *et al*. 1992), as illustrated in Fig. 8. As seen,

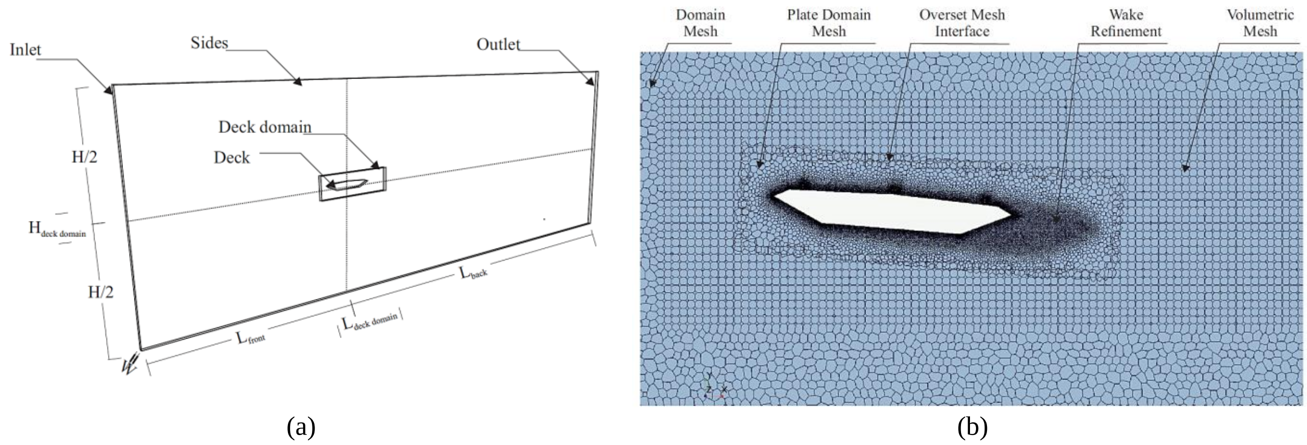

Fig. 7 Computational 3D model of the bridge deck cross-section. (a) Computational 3D domain and (b) Mesh structure

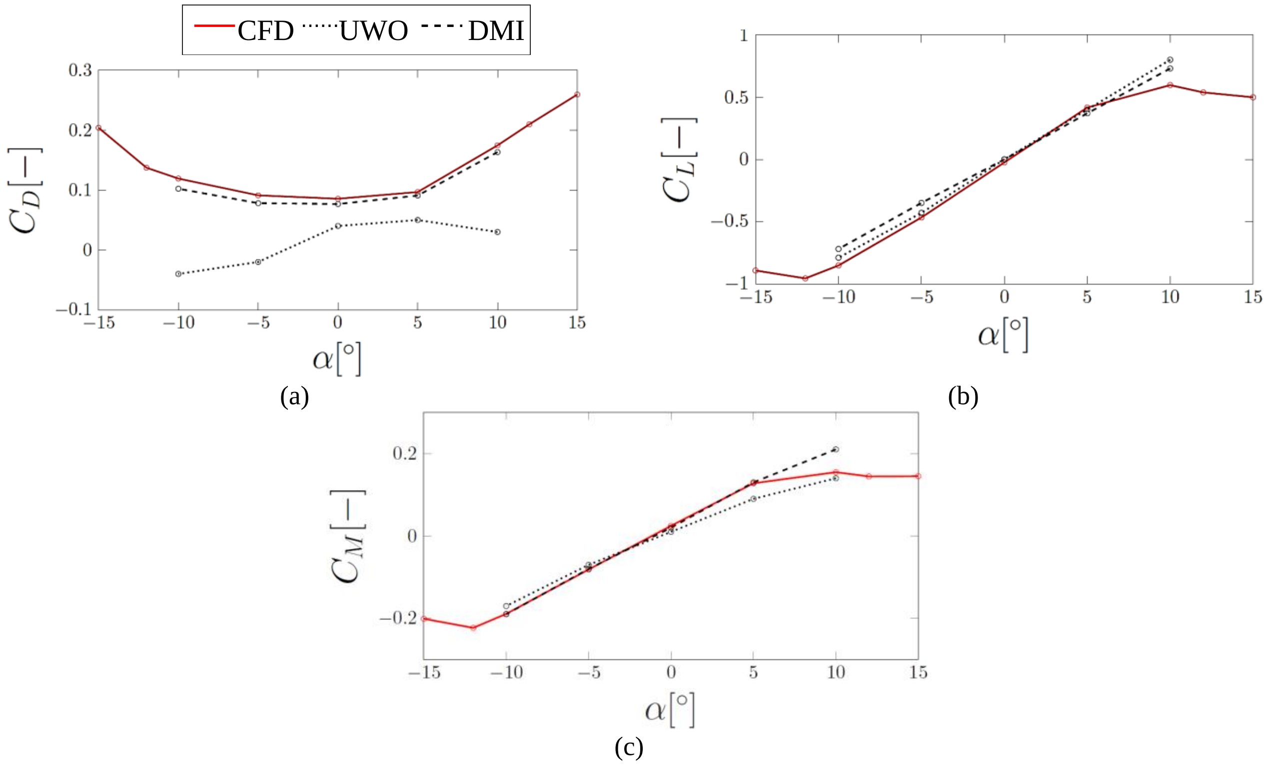

Fig. 8 Comparison of the backbone curves. (a) Drag coefficient C_D, (b) Lift coefficient C_L and (c) Moment coefficient C_M

excellent agreement is obtained between the CFD results and the wind tunnel measurements within the small angle part. In the outer range of the angle of attacks (above 10°), the backbone curves from CFD simulation show non-linear behavior as the curves flatten out. This is not seen in the wind tunnel test results, as the angles of attack during these tests were limited to ±10°. Note that the large difference in drag compared to UWO results, might be due to different railing conditions on the tested models, or due to the large difference in test method as stated in (Reinholdt *et al*. 1992). Fig. 9 shows the pressure distribution around the deck in terms of the pressure coefficients, for the angle of attack of 15° and −15°. Comparing with the unrotated configuration (zero angle of attack), rotating the deck 15° clockwise yields a bluffer body, which means the stagnation point is lowered and the high pressure affects a larger area, resulting in an increase in drag. Rotating the deck −15° (counter-clockwise), a similar flow pattern as with 15° is observed, but on the opposite faces. The projected area in the flow direction is still large, creating an increase in drag, and downward lift in this case, corresponding to the results in Fig. 8. Positive pressure is observed on most part of the top deck, but the pressure drops beneath the railings where the velocity is increased.

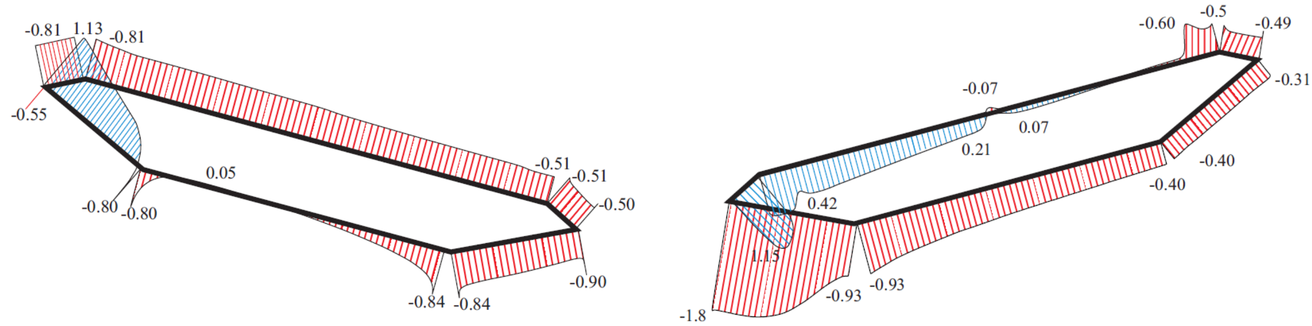

(a) (b)

Fig. 9 Pressure distribution around the deck, blue for pressure and red for suction. (a) Pressure coefficients *Cp* at 15° and (b) Pressure distribution at -15°. Railing and dividers are not shown in this figure

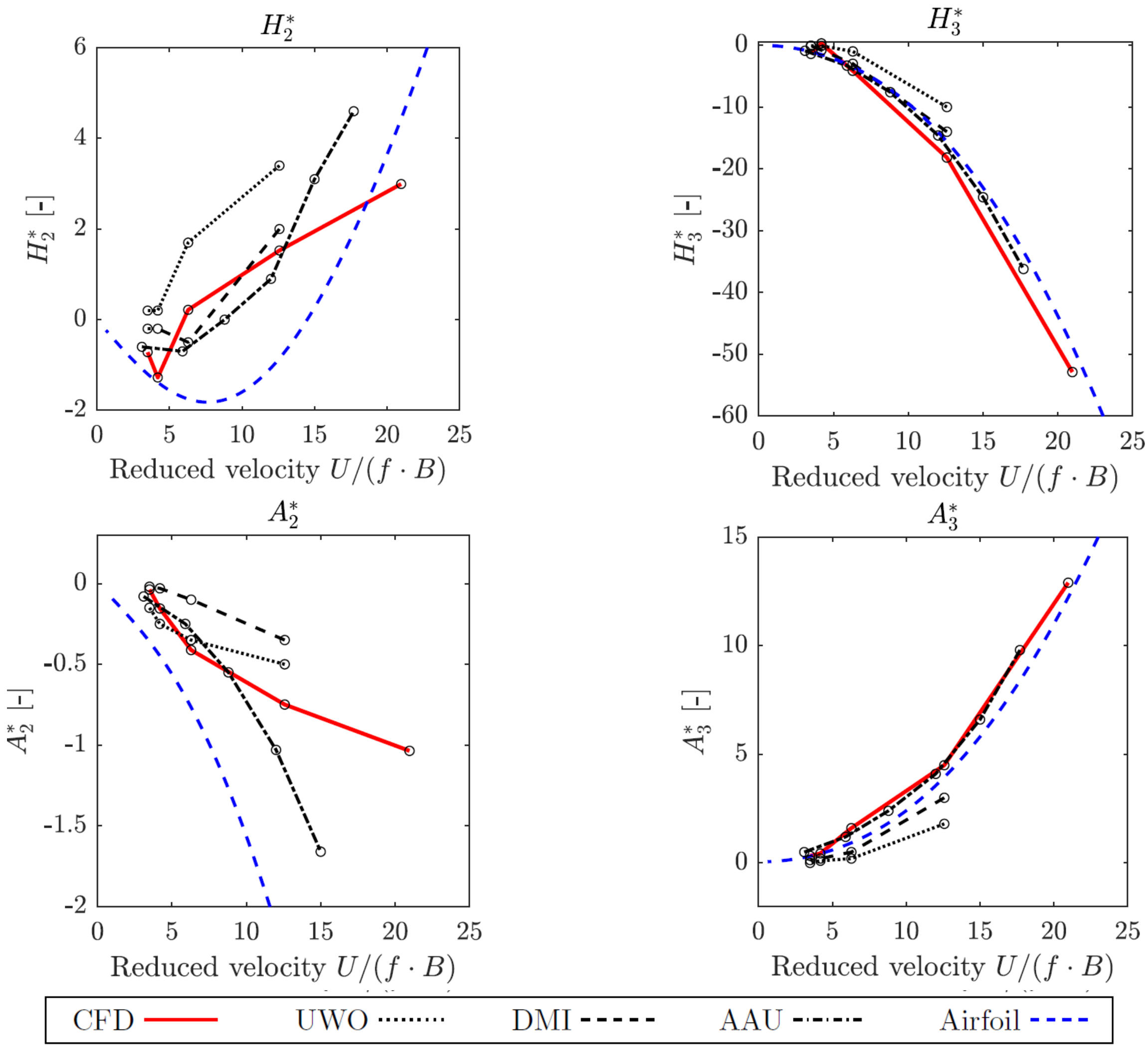

Fig. 10 Flutter derivatives related to rotation

3.3 Dynamic analysis and flutter derivatives

To obtain flutter derivatives, dynamic simulations have been conducted with two types of harmonic motions; vertical translation and torsional motion. The motion amplitudes are chosen to be the same as the ones used at UWO, being ±(1.5/300)m and ±5°, respectively. Five different reduced velocities have been used in the simulation, by changing the angular frequency ω of the harmonic motion. The flutter derivatives, which are essentially the equivalent FRFs for the aeroelastic loads due to the forced harmonic motion, have been identified using

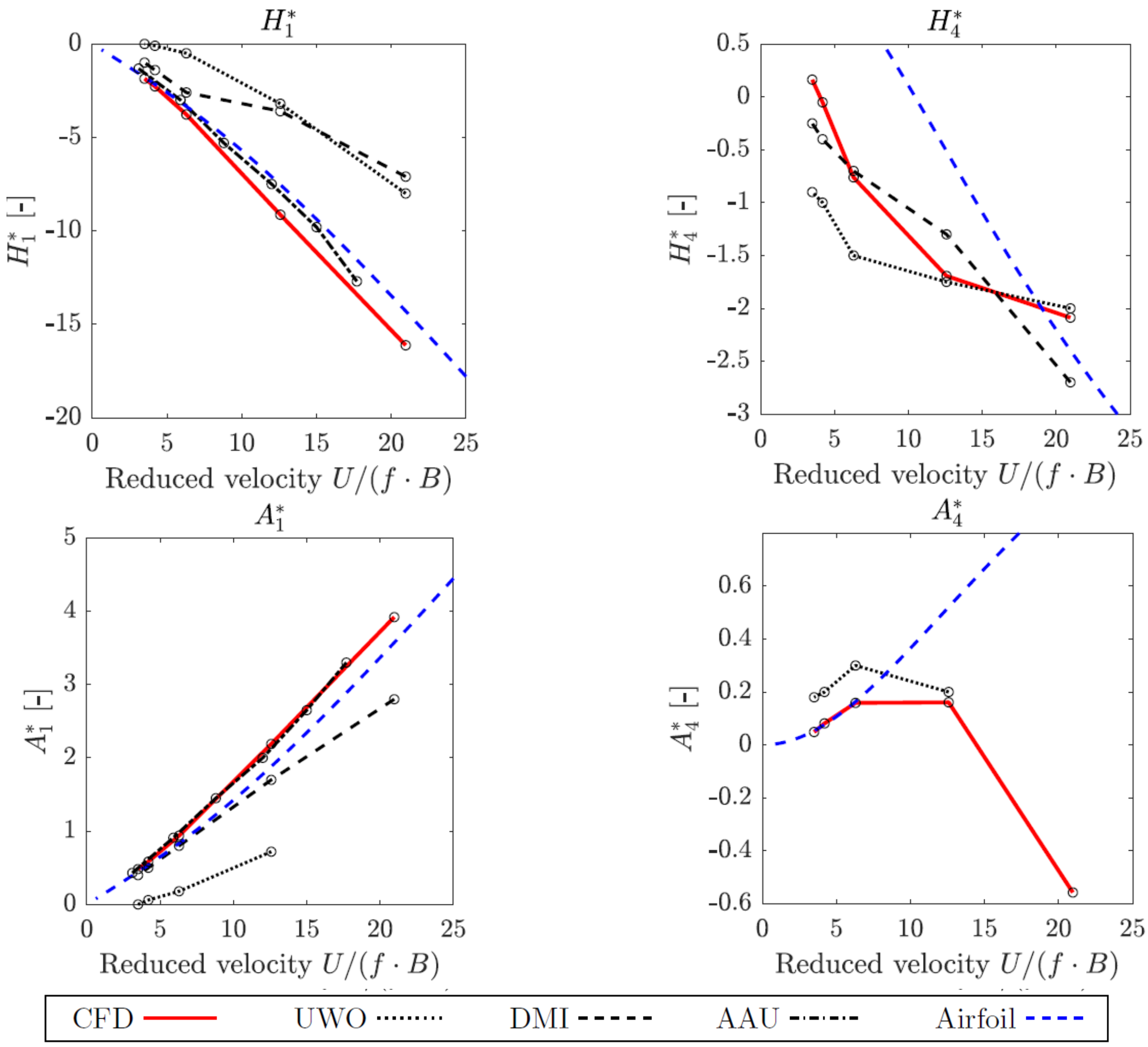

Fig. 11 Flutter derivatives related to vertical translation (heaving)

the methods described by (Chen *et al*. 2000). The amplitudes of the output (aeroelastic loads) and the input (forced harmonic motions), as well as the phase lag between them, all obtained from CFD simulations, need to be used in identifying the flutter derivatives. A minimum of four full harmonic cycles were simulated per frequency case.

The obtained flutter derivatives are illustrated in Figs. 10 and 11, together with the wind tunnel test results of DMI and UWO, as well as the results from a previous CFD study from Aalborg University (AAU) (Stærdahl *et al*. 2007) and the theoretical thin airfoil derivatives (Simiu and Scanlan 1996). It is seen that the flutter derivatives from the present study agree quite well with the measured ones from UWO and DMI, in terms of the shape of the curves. An even better agreement is observed with the results from the indicated previous CFD study although a different CFD software (EllipSys2D) was used. It is also noticeable that despite the quite different sections of a bridge and a thin airfoil, many of the derivatives are similar with largest discrepancies for derivative A_4^* relating the moment and the heaving motion.

3.4 Dynamic analysis and flutter derivatives

The nonlinear behaviors of the flow-deck system are to be revealed in this subsection, by investigating various aspects of the aeroelastic system. First, amplitude dependence on the flutter derivatives is investigated, by comparing flutter derivatives obtained from three different amplitudes of the harmonic torsional motion (input), being 3°, 5° and 10°, respectively. As shown in Fig. 12, for two of the flutter derivatives A_2^* and H_2^* the identified values are significantly changed when different amplitudes of the input motions are employed. On the other hand, the values of A_3^* and H_3^* are insensitive to the amplitudes of the input motion. It can be proved that A_2^* specifies the imaginary part of the FRF relating the torsional motion with the torsional moment, and H_2^* corresponds to the imaginary part of the FRF relating the torsional motion with the lift force. A_3^* and H_3^* are the corresponding real parts, respectively. Therefore, the imaginary parts of the FRFs are more amplitude dependent than the real parts. From a physical point of view, it means that the amplitude of the vibration has larger nonlinear influence on the aerodynamic

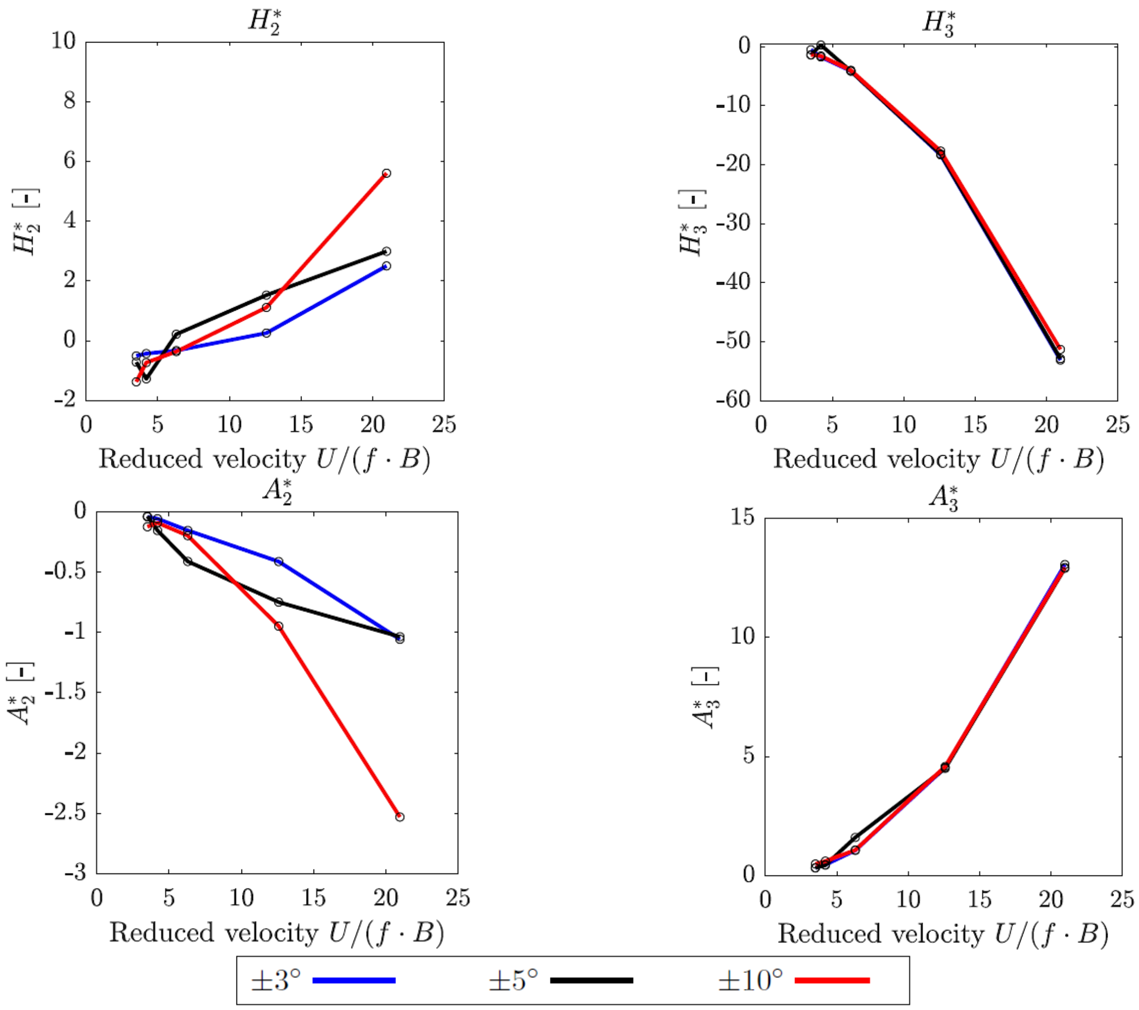

Fig. 12 Flutter derivatives for different angular amplitudes

damping than the aerodynamic stiffness. Nevertheless, the above results clearly illustrate the nonlinearity presented in the input-output relationship, which the linear semi-empirical model by Scanlan cannot cover.

Next, hysteresis loops (relating the torsional angle to the lift and moment coefficients) are analyzed by letting the bridge deck harmonically rotate around four different neutral angles α_n, being 0°, 5°, 10°, and 15°, with a constant amplitude of 5°. Three different frequencies of the harmonic motion have been evaluated, being 3Hz, 5Hz and 10Hz. Figs. 13 and 14 show the resulting hysteresis loops, together with the backbone curves (red curve) obtained from section 3.2. As seen, the hysteresis loops around 0° neutral angle are quite similar for different frequencies and are following the backbone curve. Only a small delay with respect to the static backbone curve is observed, and the flow-deck system behaves quite linearly. Larger frequency of the input motion leads to larger hysteresis loops with smaller slope (meaning more significant delay), although all loops are quite ellipsoidal in shape. Increasing the neutral angle to 5° yields a more nonlinear behavior, where larger delay with respect to the backbone curve is observed and the hysteresis loops become much more irregular. Due to delay of the flow behavior with respect to the deck motion, the hysteretic loops do not curve along the backbone curve.

This phenomenon will be treated in more detail in Section 4. Increasing the neutral angle further to 10° and 15°, the hysteresis loops becomes even more irregular with large fluctuations where a general pattern has been lost. It should be noted that in these cases, low frequency (3Hz) in the harmonic motion input leads to more significant irregularities (nonlinearity) in the hysteresis loop. This is due to the ratio between the flow velocity and the motion velocity, as the slow deck motion allows the created vortices to develop fully along the deck. This is also illustrated by the flow pattern in Fig. 15. Almost immediately after the deck begins to rotate clockwise a vortex appears at the front of the deck, which grows in size as it washes downwards. When this vortex reaches the end of the deck, a new vortex is formed at the tail of deck and sheds the larger vortex, making them both free vortices. This flow pattern cannot be seen for larger frequencies (not shown here), where the running vortex is interrupted by the deck motion before reaching the tail. Again, all the irregularities of the hysteresis loops reveal the nonlinearities presented in the aeroelastic system.

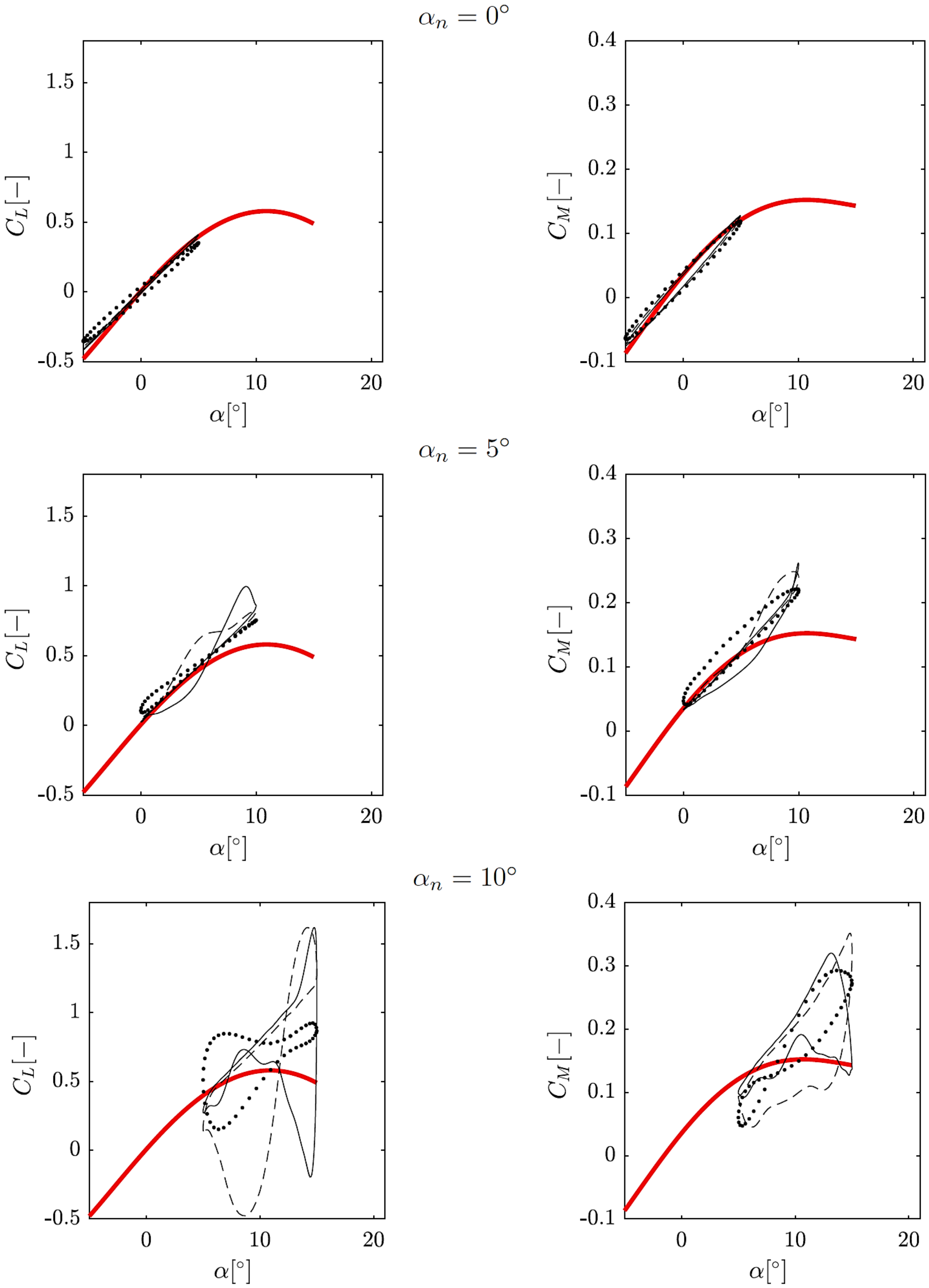

Fig. 13 Hysteresis loops around neutral angles of 0°, 5° and 10° along the lift and moment backbone curves

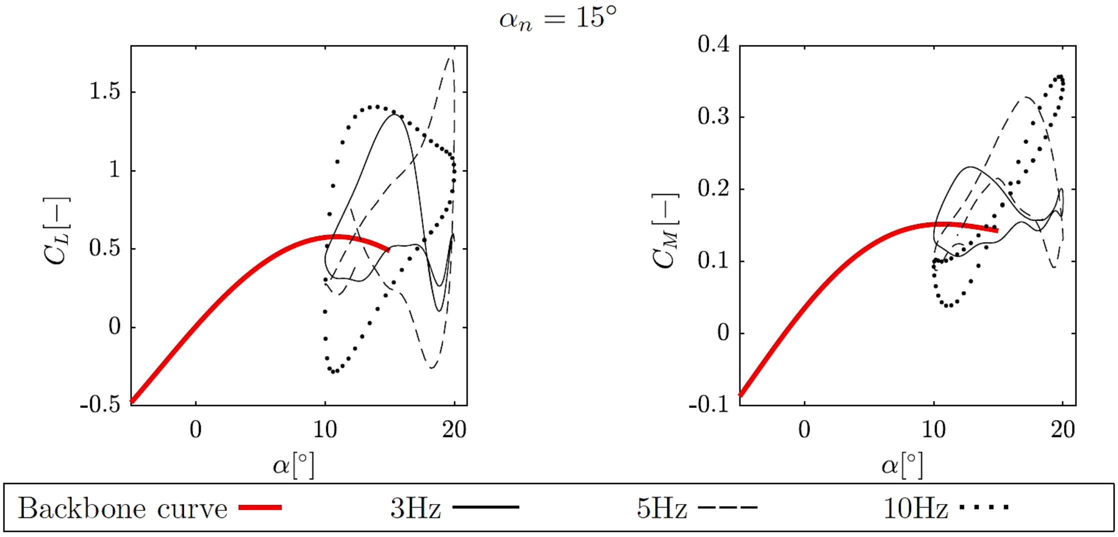

Fig. 14 Hysteresis loops around neutral angle of 15° along the lift and moment backbone curves

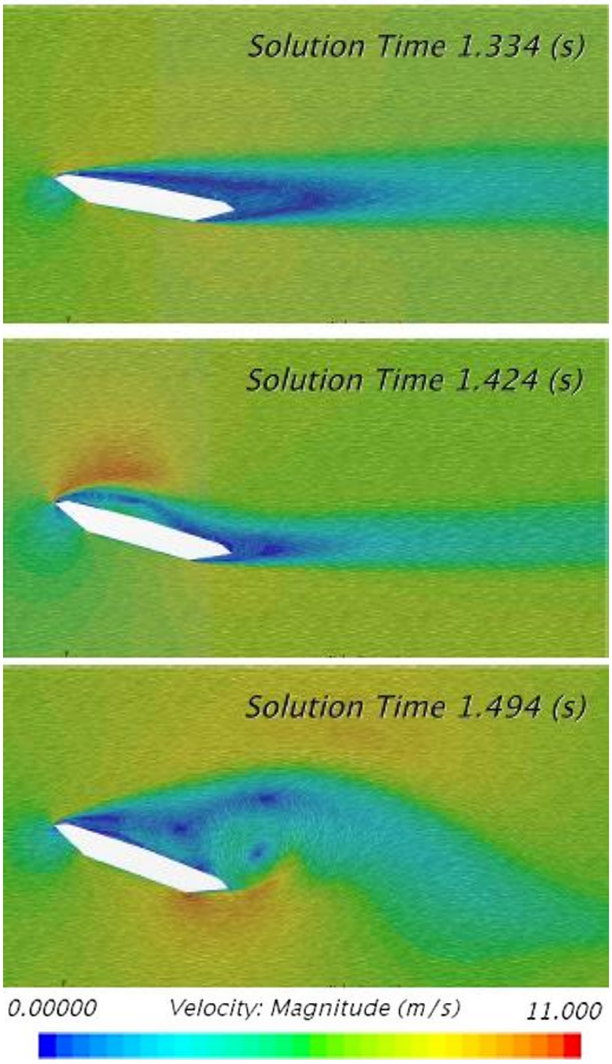

Fig. 15 Flow pattern around the deck rotating harmonically with respect to a neutral angle 15°, at a frequency of 3 Hz

4. Semi-analytical model for nonlinear aeroelastic loads

A nonlinear unsteady aeroelastic (motion-induced) load model is proposed taking into consideration the flow separation together with various delay effects, which is inspired by a dynamic stall model (only considering lift coefficient) proposed for airfoils of wind turbine blades (Larsen *et al.* 2007). Comparing with the wind turbine blade, the flow around the non-streamlined bridge deck is more complicated including separation, reattachment, interaction between the leading vortex and trailing vortex, and so on. Deriving an analytical model capturing all the indicated physical phenomenon is impossible. Instead, the proposed semi-analytical model mainly accounts for two of the most important behaviors of flow-deck system, namely the lift/moment reduction following the backbone curve (with all the nonlinear effects included), and the delayed dynamic lift/moment coefficient with respect to the nonlinear backbone curve.

4.1 Model description

The reduction of the static lift/moment coefficient with increased angle of attack can be expressed by the following equation (Larsen *et al.* 2007)

$$C_L(\alpha)=cos^4\left(\frac{\gamma_L(\alpha)}{4}\right)\cdot C_{L0}(\alpha)$$
$$C_M(\alpha)=cos^4\left(\frac{\gamma_M(\alpha)}{4}\right)\cdot C_{M0}(\alpha) \tag{2}$$

where $C_L(\alpha)$ = $C_L(\alpha(t))$ and $C_M(\alpha)$ = $C_M(\alpha(t))$ are the static lift and moment coefficients (without time delay) following the nonlinear backbone curves, and $\alpha(t)$ is the angle of attack of the deck at the present time. $C_{L0}(\alpha)$ = $C_{L0}(\alpha(t))$ and $C_{M0}(\alpha)$ = $C_{M0}(\alpha(t))$ are the static lift and moment coefficients which are linearly dependent of α, corresponding to the so-called fully attached flow for airfoils. For bridge decks, $C_{L0}(\alpha)$ and $C_{M0}(\alpha)$ are straight lines following the initial slope at zero angle of attack of the backbone curves. $\gamma_L(\alpha)$ = $\gamma_L(\alpha(t))$ and $\gamma_M(\alpha)$ = $\gamma_M(\alpha(t))$ are the parameters (derived from conformal mapping) describing the attachment degree, or location of the separation point, for the wind turbine airfoil (Larsen *et al*. 2007), where zero value corresponds to full attachment. For the bridge deck, $\gamma_L(\alpha)$ and $\gamma_M(\alpha)$ indicate the reduction of static lift and moment with respect to $C_{L0}(\alpha)$ and $C_{M0}(\alpha)$, respectively, due to nonlinear flow behavior. Thus $\gamma_L(\alpha)$ = $\gamma_M(\alpha)$ = 0 corresponds to the case of zero angle of attack. The relationship between $\gamma_L(\alpha)$ and α and the relationship between $\gamma_M(\alpha)$ and α can be calibrated from the backbone curves in Fig. 8.

Next, the unsteady flow characteristics are to be modelled by two delay effects. First, according to classical aeroelasticity theory (Fung 2002), the increment dC_{L0} of the linear lift due to an increment $d\alpha$ of the angle of attack is not achieved instantaneously. This delay can be modelled via the introduction of an indicial function (unit-step response function) $\Phi_L(t)$. Same argument can be made to the linear moment coefficient. Therefore, the increment $dC_{L0,d}$ or $dC_{M0,d}$ at t due to an increment $d\alpha(\tau)$ at an earlier time τ can be written as

$$dC_{L0,d}(t)=\Phi_L(t-\tau)\, dC_{L0}(\tau)$$
$$dC_{M0,d}(t)=\Phi_M(t-\tau)\, dC_{M0}(\tau) \tag{3}$$

Upon superposition of the effects of all previous increments, the dynamic linear lift $C_{L0,d}(t)$ and the dynamic linear moment $C_{M0,d}(t)$ are given as

$$C_{L0,d}(t)=\int_{-\infty}^{t}\Phi_L(t-\tau)\dot{C}_{L0}(\tau)d\tau$$
$$C_{M0,d}(t)=\int_{-\infty}^{t}\Phi_M(t-\tau)\dot{C}_{M0}(\tau)d\tau \tag{4}$$

The analytical expression of $\Phi_L(t)$ can be derived for streamlined airfoils known as the Wagner function. For bridge decks, the indicial functions $\Phi_L(t)$ and $\Phi_M(t)$ depend on the cross-section, and an approximated semi-analytical expression needs to be proposed. $\Phi_L(t)$ and $\Phi_M(t)$ are assumed to fulfill $0 < \Phi_L(t) \leq 1$,$0 < \Phi(t)_M \leq 1$ and $\Phi_L(\infty)$ = $\Phi_M(\infty)$ = 1 indicating the flow is completely settled down with infinitely long time. For the bridge deck, overshooting of the indicial functions with respect to unity might take place. However, this is neglected in the present study. With the similar format as Jones' approximation to the Wagner function, the following first-order filter expressions are proposed for $\Phi_L(t)$ and $\Phi_M(t)$ in the present study

$$\Phi_L(t)=1-a_{L,1}e^{-b_{L,1}t}-a_{L,2}e^{-b_{L,2}t}$$
$$\Phi_M(t)=1-a_{M,1}e^{-b_{M,1}t}-a_{M,2}e^{-b_{M,2}t} \tag{5}$$

where the positive coefficients $a_{L,1}$, $a_{L,2}$, $b_{L,1}$, $b_{L,2}$, $a_{M,1}$, $a_{M,2}$, $b_{M,1}$, $b_{M,2}$ need to be calibrated from wind tunnel tests or CFD simulations (as is done in the present paper). In principle additional exponential terms can be added to the right hand side of Eq. (5) for better representing the test or simulation results, but more parameters need to be calibrated accordingly. Combining Eqs. (4) and (5) and after some derivation, the dynamic linear lift $C_{L0,d}(t)$ and the dynamic linear moment $C_{M0,d}(t)$ can be obtained by the following output equations

$$C_{L0,d}(t)=C_{L0}(t)-x_{L,1}(t)-x_{L,2}(t)$$
$$C_{M0,d}(t)=C_{M0}(t)-x_{M,1}(t)-x_{M,2}(t) \tag{6}$$

where $C_{L0}(t)$ and $C_{M0}(t)$ are the static linear lift coefficient and static linear moment coefficient described above. $x_{L,1}(t)$, $x_{L,2}(t)$, $x_{M,1}(t)$, $x_{M,2}(t)$ are the state variables related to the filter, which are defined and can be solved by the first-order differential equations

$$\dot{x}_{L,1}(t)+b_{L,1}x_{L,1}(t)=a_{L,1}\dot{C}_{L0}(t)$$
$$\dot{x}_{L,2}(t)+b_{L,2}x_{L,2}(t)=a_{L,2}\dot{C}_{L0}(t)$$
$$\dot{x}_{M,1}(t)+b_{M,1}x_{M,1}(t)=a_{M,1}\dot{C}_{M0}(t)$$
$$\dot{x}_{M,2}(t)+b_{M,1}x_{M,2}(t)=a_{M,2}\dot{C}_{M0}(t) \tag{7}$$

The second delay effect is related to the unsteady nonlinear flow behavior, i.e., delay of the nonlinear lift/moment reduction. This is to account for the unsteadiness of all the nonlinear effects present in the flow-deck system. This delay effect is modelled by the following 1st order filter equation acting on $\gamma_L(\alpha(t))$ and $\gamma_M(\alpha(t))$

$$\begin{aligned}\dot{\gamma}_{L,d}(t)&=-b_{L,3}\left[\gamma_{L,d}(t)-\gamma_L(t)\right]\\ \dot{\gamma}_{M,d}(t)&=-b_{M,3}\left[\gamma_{M,d}(t)-\gamma_M(t)\right]\end{aligned}\tag{8}$$

where $b_{L,3}$ and $b_{M,3}$ are constant coefficients that need to be calibrated from CFD simulations together with $a_{L,1}$, $a_{L,2}$, $b_{L,1}$, $b_{L,2}$, $a_{M,1}$, $a_{M,2}$, $b_{M,1}$, $b_{M,2}$. Calibration of the parameters for lift and moment are done separately. Direct numerical search has been performed, i.e., the best fit between the theoretical model and CFD results is searched by changing the values of coefficients so that the standard deviation of the difference is minimized. In principle, more rigorous optimization algorithms can be used for the coefficients calibration. $\gamma_{L,d}(t)$ and $\gamma_{M,d}(t)$ are the dynamic parameters for lift and moment reductions, respectively, accounting for the delay effect with respect to $\gamma_L(t)$ and $\gamma_M(t)$.

In matrix formulation, the linear differential equations Eqs. (7) and (8) describing these six state variables can be organized in the following state vector formulation

$$\dot{\mathbf{y}}(t)=\mathbf{A}_1\mathbf{y}(t)+\mathbf{u}_1(t)\tag{9}$$

where

$$\mathbf{y}(t)=\begin{bmatrix}x_{L,1}(t)\\x_{L,2}(t)\\\gamma_{L,d}(t)\\x_{M,1}(t)\\x_{M,2}(t)\\\gamma_{M,d}(t)\end{bmatrix}\qquad \mathbf{u}_1(t)=\begin{bmatrix}a_{L,1}\,\dot{C}_{L0}(t)\\a_{L,2}\,\dot{C}_{L0}(t)\\b_{L,3}\,\gamma_L(t)\\a_{M,1}\,\dot{C}_{M0}(t)\\a_{M,2}\,\dot{C}_{M0}(t)\\b_{M,3}\,\gamma_M(t)\end{bmatrix}$$

$$\mathbf{A}_1=\begin{bmatrix}-b_{L,1}&0&0&0&0&0\\0&-b_{L,2}&0&0&0&0\\0&0&-b_{L,3}&0&0&0\\0&0&0&-b_{M,1}&0&0\\0&0&0&0&-b_{M,2}&0\\0&0&0&0&0&-b_{M,3}\end{bmatrix}\tag{10}$$

where $\mathbf{y}(t)$ is the aeroelastic state vector containing the six state variables. $\dot{C}_{L0}(t)$, $\dot{C}_{M0}(t)$, $\gamma_M(t)$ and $\gamma_L(t)$ are the inputs to Eq. (9), which are known functions of the instantaneous angle of attack $\alpha(t)$ from the backbone curves. It should be noted that if more exponential terms are added to the right-hand side of Eq. (5) for better representing the CFD results, the dimension of the aeroelastic state vector $\mathbf{y}(t)$ will be larger.

Finally, the dynamic (unsteady) form of Eq. (2) can be written as

$$\begin{aligned}C_{L,d}(t)&=\cos^4\left(\frac{\gamma_{L,d}(t)}{4}\right)\cdot\left(C_{L0}(\alpha(t))-x_{L,1}(t)-x_{L,2}(t)\right)\\ C_{M,d}(t)&=\cos^4\left(\frac{\gamma_{M,d}(t)}{4}\right)\cdot\left(C_{M0}(\alpha(t))-x_{M,1}(t)-x_{M,2}(t)\right)\end{aligned}\tag{11}$$

where $C_{L,d}(t)$ and $C_{M,d}(t)$ are the final unsteady lift and moment coefficients that we are looking for. $x_{L,1}(t)$, $x_{L,2}(t)$, $\gamma_{L,d}(t)$, $x_{M,1}(t)$, $x_{M,2}(t)$ and $\gamma_{M,d}(t)$ are the six aeroelastic state variables solved from Eq. (9).

4.2 Procedure of implementing the model in flutter analysis

The presented semi-analytical model has three main advantages. First, rather than a pure fitting methodology, this model preserves certain physical explanations of the nonlinear flow-deck system, i.e. the nonlinear backbone curve of the static aerodynamic coefficient representing the flow separation, and the delayed dynamic coefficient (with respect to the backbone curve) representing the unsteady flow conditions. Second, this model is established in the state-space form, and the time-domain expressions Eqs. (9) and (11) can be easily incorporated into the equations of motion of the bridge deck and solved simultaneously. Third, the coefficients in the model are frequency-independent, which means calibration and application of this model is much more efficient than the widely-used semi-empirical model (with flutter derivatives).

In most cases, the bridge deck motion is modeled as a two-degree-of-freedom system with vertical and rotational motions $h(t)$ and $\theta(t)$, and the equations of motion are given by

$$\begin{aligned}m\left(\ddot{h}+2\zeta_h\omega_h\dot{h}+\omega_h^2h\right)&=-\frac{1}{2}\rho V^2B\,C_{L,d}(\alpha_i)\\ I\ddot{\theta}+2\zeta_\theta\omega_\theta\dot{\theta}\left(\omega_\theta^2+\theta\right)&=\frac{1}{2}\rho V^2B^2C_{M,d}(\alpha_i)\end{aligned}\tag{12}$$

where ω and ζ denote the angular eigenfrequency and damping ratio of the deck, respectively. m is the effective mass and I is the effective mass moment of inertia. The two terms on the right-hand side of the equations are the aerodynamic/aeroelastic force and moment, respectively. $C_{L,d}(\alpha_i)$ and $C_{M,d}(\alpha_i)$ are the unsteady lift and moment coefficients as calculated by Eq. (11), where the instantaneous angle of attack $\alpha_i(t)$ is used here. $\alpha_i(t)$ is generally defined:

$$\alpha_i(t)=\theta+\tan^{-1}\left(\frac{W+w+\dot{h}+m_1B\dot{\theta}}{V+v}\right)\tag{13}$$

where V is the mean wind velocity in the horizontal direction, and W is the mean wind velocity in the vertical direction (normally W = 0). v and w are the corresponding turbulence fluctuations. h and θ are the deck motions as in Eq. (12). The parameter m_1 takes into account averaged angular velocity-induced effect, the value of which is 0.25 for streamlined airfoil and fall between -0.5 and 0.5 for bluff-body sections (Wu and Kareem 2013b). In principle the proposed model becomes equivalent to the thin-airfoil theory, if 1) both the backbone curves and Eq. (13) are linearized around zero angle of attack, and 2) Wagner function is used as the induction functions in Eq. (4).

At each time instant, $\alpha_i(t)$ can be calculated from Eq. (13), and the unsteady aerodynamic coefficient can then be calculated using Eq. (11) if the aeroelastic state vector $\mathbf{y}(t)$ has been solved from Eq. (9). This can be done by combining Eqs. (9) and (12) into an extended state vector form

$$\dot{\mathbf{z}}(t)=\mathbf{A}\mathbf{z}(t)+\mathbf{u}(t) \tag{14}$$

where

$$\mathbf{z}(t)=\begin{bmatrix} h(t) \\ \theta(t) \\ \dot{h}(t) \\ \dot{\theta}(t) \\ y(t) \end{bmatrix} \qquad \mathrm{u}(t)=\begin{bmatrix} 0 \\ -\tfrac{1}{2}\rho V^2 B\, C_{L,d}(\alpha_i) \\ 0 \\ \tfrac{1}{2}\rho V^2 B^2\, C_{M,d}(\alpha_i) \\ \mathbf{u}_1(t) \end{bmatrix}$$

$$\mathbf{A}_1=\begin{bmatrix} -b_{L,1} & 0 & 0 & 0 & 0 & 0 \\ 0 & -b_{L,2} & 0 & 0 & 0 & 0 \\ 0 & 0 & -b_{L,3} & 0 & 0 & 0 \\ 0 & 0 & 0 & -b_{M,1} & 0 & 0 \\ 0 & 0 & 0 & 0 & -b_{M,2} & 0 \\ 0 & 0 & 0 & 0 & 0 & -b_{M,3} \end{bmatrix} \tag{15}$$

$\mathbf{z}(t)$ is the 10-dimensional extended state vector containing the deck motions as well as the aeroelastic state vector $\mathbf{y}(t)$. Flutter analysis of the bridge deck can be carried out directly in the time domain by solving Eq. (14), where nonlinear unsteady aeroelastic lift and moment have been included.

4.3 Results from the model

In the present study, the semi-analytical model for the nonlinear unsteady aeroelastic lift and moment, as described in section 4.1, are evaluated by comparing with the CFD results. Eq. (9) was solved using the 4th order Runge Kuttas method. The ten coefficients $a_{L,1}$, $a_{L,2}$, $b_{L,1}$, $b_{L,2}$, $b_{L,3}$ and $a_{M,1}$, $a_{M,2}$, $b_{M,1}$, $b_{M,2}$, $b_{M,3}$ used in the model have been calibrated to the CFD results of harmonically rotating the deck around neutral angles of 0° and 5° with a frequency of 10 Hz. Table 3 presents the calibrated values of these coefficients. Here ’^’ indicates that the coefficients have been normalized by a factor $B/2U$.

Fig. 16(a) shows the comparison of the motion-induced lift between the proposed semi-analytical model and the CFD simulation, for the case where the deck is harmonically rotating at 0° neutral angle with a frequency of 10 Hz. The lift hysteresis loop from the semi-analytical model agrees very well with that obtained from CFD. Both the nonlinear (reduced slope at the two ends) and unsteady effects have been captured. It should be mentioned that the nonlinear behavior, as revealed by the curved hysteresis loop, cannot be captured by the flutter derivatives based semi-empirical model. Fig. 16(b) presents the corresponding comparison for the case where the neutral angle is increased to 5°. Reasonable agreement is still obtained between the semi-analytical model and CFD simulation, although some deviation is found at the left side of the hysteresis loop. As already seen in Fig. 13, relatively large motion frequency (10 Hz) leads to large delay of the motion-induced load, and the hysteresis loop does not curve along the backbone curve. This is fully captured by the semi-analytical model.

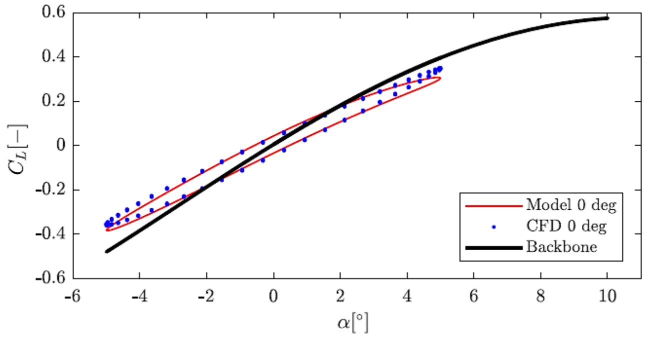

(a)

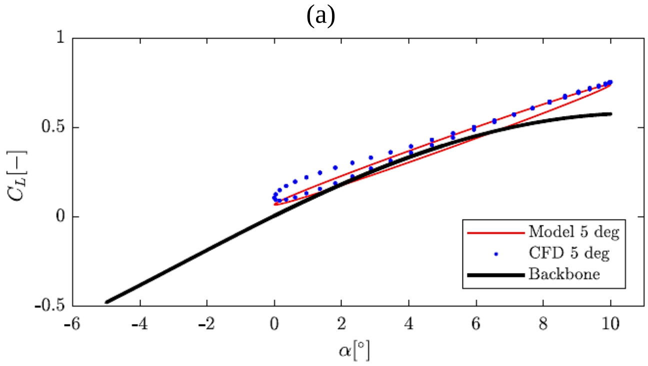

(b)

Fig. 16 Comparison of the motion-induced lift hysteresis loop between the proposed model and the CFD simulation for frequency 10 Hz, (a) 0° neutral angle and (b) 5° neutral angle

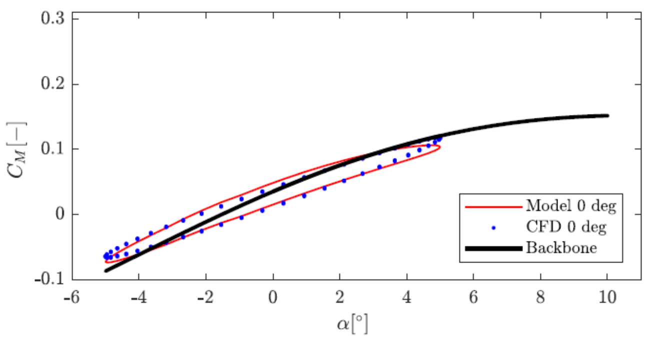

(a)

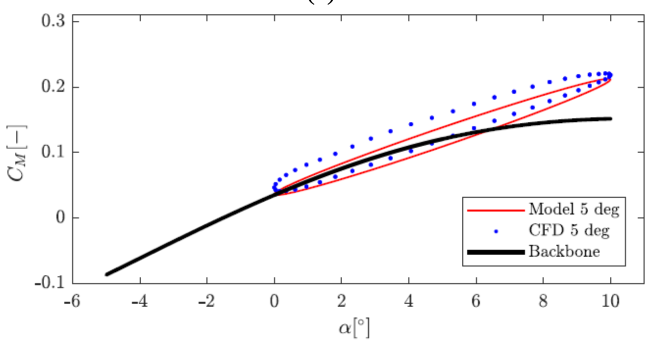

(b)

Fig. 17 Comparison of the motion-induced moment hysteresis loop between the proposed model and the CFD simulation for frequency 10 Hz, (a) 0° neutral angle and (b) 5° neutral angle

Table 3 The calibrated coefficients of the model

Coeff. (Lift)	$a_{L,1}$	$a_{L,2}$	$\hat{b}_{L,1}$	$\hat{b}_{L,2}$	$\hat{b}_{L,3}$
Value	0.20	0.15	1.7	0.15	0.01
Coeff. (Moment)	$a_{M,1}$	$a_{M,2}$	$\hat{b}_{M,1}$	$\hat{b}_{M,2}$	$\hat{b}_{M,3}$
Value	0.15	0.40	1.5	1.5	0.006

Table 4 Area enclosed by the hysteresis loops for frequency 10 Hz

	α_n [°]	C_L	C_M
CFD	0	0.613	0.227
Model	0	0.608	0.261
CFD	5	0.329	0.325
Model	5	0.503	0.230

Furthermore, Table 4 summarizes the area enclosed by the hysteresis loops (both lift and moment) obtained from the model and CFD. In general, the enclosed area agrees well between the model and CFD, especially for the case around 0° neutral angle. The model over-predicts the area of C_L and underestimates the area of C_M, around 5°, as already illustrated by Figs. 16 and 17. The enclosed area of C_M hysteresis loop exactly demonstrates the work done by the aeroelastic loads during one period of the deck rotation. Since the motion-induced moment is delayed with respect to the angle of attack, larger area of the loop indicates larger energy dissipation.

Next, Fig. 18 shows the results of the motion-induced lift for the case where the deck is harmonically rotating with a frequency of 5 Hz. When the motion frequency is decreased, the flow behaves more nonlinear (due to the very bluff nature of this configuration) and the hysteresis loops from CFD are seen to be rather irregular. Further, the coefficients of the semi-analytical model as in Table 3 have been calibrated by the case of 10 Hz motion frequency. Therefore, the agreement between the model and CFD in this case is much poorer than that in Fig. 16. The semi-analytical model predicts a larger loop than CFD in Fig. 18(a), and is not able to reproduce the irregular loop obtained from CFD in Fig. 18(b). Nevertheless, the model well predicts the general tendency of the hysteresis loops. Here, it should also be noted that 5 Hz is a relatively low frequency for the scaled deck model (1:300). Fig. 19 shows the corresponding moment hysteresis loops for the 5 Hz motion frequency. Around 0° neutral angle, the results obtained from the moment model generally agree with that from CFD as seen in Fig. 19(a). The narrowed-down hysteresis loop comparing with that in Fig. 17(a) is also well predicted by the semi-analytical model. However, the moment model fails to predict the highly irregular hysteresis loop for the case around 5° neutral angle in Fig. 19b), although the same slope of the hysteresis loop matches well.

Finally, Table 5 summarizes the area enclosed by the hysteresis loops (both lift and moment) obtained from the model and CFD, for 5 HZ motion frequency. The agreement is poorer than that in Table 4, especially for lift hysteresis loop around 0° neutral angle. Comparing with Table 4, all the moment hysteresis loops exhibit smaller area indicating smaller energy dissipation at lower frequency. This is well captured by the semi-analytical model.

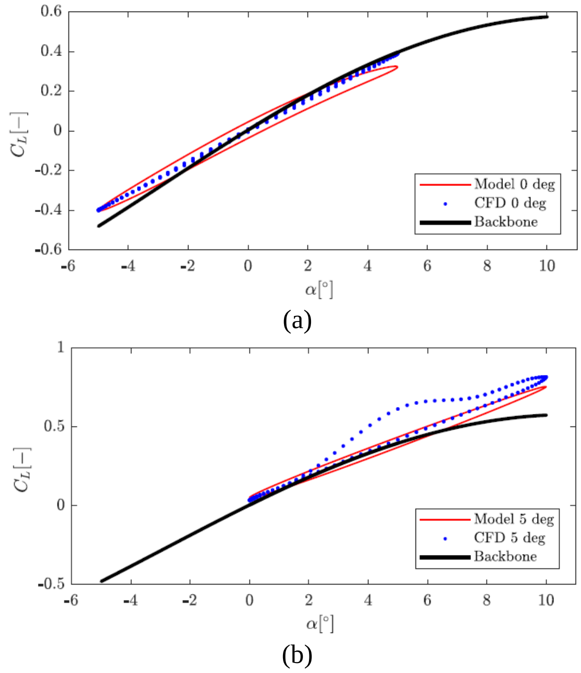

Fig. 18 Comparison of the motion-induced lift hysteresis loop between the proposed model and the CFD simulation for frequency 5 Hz, (a) 0° neutral angle and (b) 5° neutral angle

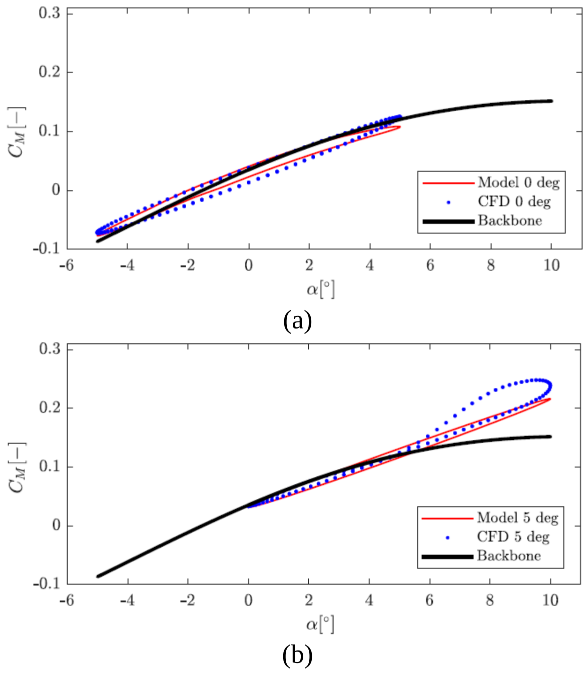

Fig. 19 Comparison of the motion-induced moment hysteresis loop between the proposed model and the CFD simulation for frequency 5 Hz, (a) 0° neutral angle and (b) 5° neutral angle

Table 5 Area enclosed by the hysteresis loop for frequency 5 Hz

	α_n [°]	C_L	C_M
CFD	0	0.088	0.194
Model	0	0.640	0.139
CFD	5	0.890	0.173
Model	5	0.510	0.118

In general, the semi-analytical model reasonably captures the main characteristics of CFD results in terms of the shape and enclosed area of the hysteresis loop, especially for the cases where the CFD results exhibit well-defined hysteresis loops. These correspond to the weakly nonlinear flow-deck system. For the cases of large neutral angle and low motion frequency, the hysteresis loops from the CFD become highly irregular, and the proposed model is not able to capture this significantly nonlinear effect. Still, this model is in nature nonlinear and unsteady, and it shows high potential for further refinement and application in aeroelastic analysis of bridges. The high irregularities of the hysteresis loop at high neutral angles might be better captured by adding more terms on the right-hand side of Eq. (5), leading to a more complicated model with more coefficients to be calibrated, as well as larger dimension of the aeroelastic state vector $\mathbf{y}(t)$ in Eq. (9).

5. Conclusions

In this paper, series of CFD simulations have been carried out to investigate aeroelasticity of the GBEB bridge deck, with a focus on the nonlinear behaviors of the aeroelastic system. Careful verification and validation of the computational schemes have been performed before extensive simulations on GBEB. Static aerodynamic coefficients of the deck have been calculated at various angles of attack, leading to the nonlinear backbone curve. Flutter derivatives of the bridge are then identified by CFD simulations using forced harmonic motion of the cross-section with various frequencies. By varying the amplitude of the harmonic deck motion, it is found that the identified flutter derivatives are highly amplitude dependent, especially for A_2^* and H_2^* parameters corresponding to the imaginary parts of the aeroelastic FRFs. Nonlinear feature in the flow-deck system has also been observed from the change of hysteresis loop (between angle of attack and lift/moment) when the neutral angles of the cross-section are changed. For high neutral angles, the hysteresis loops become very irregular due to highly complicated flow behavior, especially for low frequencies of the deck motion.
Based on the observed nonlinear aeroelastic behavior from CFD simulations, a reduced order semi-analytical model for the aeroelastic loads has been proposed, accounting for both the nonlinear and unsteady effects. The model is derived to represent the two most important features, the lift/moment reduction following the backbone curve (with all the nonlinear effects included), and the delayed dynamic lift/moment with respect to the nonlinear backbone curve. A state vector formulation has been established for the first order differential equations with a six-dimensional aeroelastic state vector, based on which the nonlinear unsteady lift/moment can be obtained. In this way, the model can be easily incorporated into the deck equations of motion and solved in the time domain for flutter analysis. The results from this semi-analytical model generally agree well with those from CFD simulations in terms of the shape and enclosed area of the weakly nonlinear hysteresis loops, as long as the loops obtained from CFD are well-defined. For the case of large neutral angle with small motion frequency where hysteresis loops are highly irregular, this model is not able to reproduce this highly nonlinear effect and larger deviations are found. It is believed that further refinement of the semi-analytical model can be made by including more terms and more coefficients to be calibrated, in order to better represent the irregular aeroelastic system. Flutter analysis of the bridge using the proposed nonlinear model will also be investigated in a future study.

References

Bruno, L. and Mancini, G. (2002), “Importance of deck details in bridge aerodynamics”, *Struct. Eng. Int.*, **12**(4), 289-294.

Brusiani, F., De Miranda, S., Patruno, L., Ubertini, F. and Vaona, P. (2013), “On the evaluation of bridge deck flutter derivatives using RANS turbulence models”, *J. Wind Eng. Ind. Aerod.*, **119**, 39-47.

Chen, X. and Kareem, A. (2003), “Aeroelastic analysis of bridges: Effects of turbulence and aerodynamic nonlinearities”, *J. Eng. Mech.*, **129**(8), 885-895.

Chen, X., Matsumoto, M. and Kareem, A. (2000), “Time domain flutter and buffeting response analysis of bridges”, *J. Eng. Mech.*, **126**(1), 7-16.

Davenport, A.G., King, J.P.C. and Larose, G.L. (1992), “Taut strip model tests”, *Aerod. Large Brid.*, 113-124.

Demartino, C. and Ricciardelli, F. (2017), “Aerodynamics of nominally circular cylinders: A review of experimental results for Civil Engineering applications”, *Eng. Struct.*, **137**, 76-114.

Diana G., Bruni S., Cigada A. and Collina A. (1993), “Turbulence effect on flutter velocity in long span suspended bridges”, *J. Wind Eng. Ind. Aerod.*, **48**(2-3), 329-342.

Diana, G., Resta, F. and Rocchi, D. (2008), “A new numerical approach to reproduce bridge aerodynamic non-linearities in time domain”, *J. Wind Eng. Ind. Aerod.*, **96**(10), 1871-1884.

Diana, G., Rocchi, D., Argentini, T. and Muggiasca, S. (2010), “Aerodynamic instability of a bridge deck section model: Linear and nonlinear approach to force modeling”, *J. Wind Eng. Ind. Aerod.*, **98**(6), 363-374.

Dutta, S., Panigrahi, P.K. and Muralidhar, K. (2008), “Experimental investigation of flow past a square cylinder at an angle of incidence”, *J. Eng. Mech.*, **134**(9), 788-803.

Fung, Y.C. (2002), *An Introduction to the Theory of Aeroelasticity*, Courier Corporation.

Guo, J., Zheng, S., Zhu, J., Tang, Y. and Hong, C. (2017), “Study on post-flutter state of streamlined steel box girder based on 2 DOF coupling flutter theory”, *Wind Struct.*, **25**(4), 343-360.

Kovacs, I., Svensson, H. and Jordet, E. (1992), “Analytical aerodynamic investigation of cable-stayed Helgeland bridge”, *J. Struct. Eng.*, **118**(1), 147-168.

Larsen, J.W., Nielsen, S.R.K. and Krenk, S. (2007), “Dynamic stall model for wind turbine airfoils”, *J. Fluid Struct.*, **23**(7), 959-982.

Liaw, K. (2005), Simulation of flow around bluff bodies and bridge deck sections using CFD, *Doctoral dissertation*, *University of Nottingham*.

Lysenko, D.A., Ertesvåg, I.S. and Rian, K.E. (2012), "Large-eddy simulation of the flow over a circular cylinder at Reynolds number 3900 using the OpenFOAM toolbox", *Flow Turbul. Combust.*, **89**(4), 491-518.

Mannini, C., Sbragi, G. and Schewe, G. (2016), "Analysis of self-excited forces for a box-girder bridge deck through unsteady RANS simulations", *J. Wind Eng. Ind. Aerod.*, **63**, 57-76.

Menter, F.R., Kuntz, M. and Langtry, R. (2003), "Ten years of industrial experience with the SST turbulence model", *Turbul. Heat Mass Trans,* **4**(1), 625-632.

Nieto, F., Hernandez, S., Jurado, J.A. and Baldomir, A. (2010), "CFD practical applicaion in conceptual design of a 425 m cable-stayed bridge", *Wind Struct.*, **13**(4), 309-326.

Patruno, L. (2015), "Accuracy of numerically evaluated flutter derivatives of bridge deck sections using RANS: Effects on the flutter onset velocity", *Eng. Struct.*, **89**, 49-65.

Reinhold, T.A., Brinch, M. and Damsgaard, A. 1992, "Wind-Tunnel tests for the Great Belt Link", *Aerod. Large Brid.*, 255-267.

Saha, A.K., Biswas, G. and Muralidhar, K. (2003), "Three-dimensional study of flow past a square cylinder at low Reynolds numbers", *Int. J. Heat Fluid Fl.*, **24**(1), 54-66.

Scanlan, R.H. (1978), "The action of flexible bridges under wind, 1: Flutter theory, *J. Sound Vib.*, **60**(2), 187-199.

Simiu, E. and Scanlan, R.H. (1996), *Wind Effects on Structures*, Wiley.

Stæ rdahl, J.W., Sørensen, N.N. and Nielsen, S.R.K. (2007), "Aeroelastic stability of suspension bridges using CFD", *Proceedings of the IASS Symposium*.

Starossek, U., Aslan, H. and Thiesemann, L. (2009), "Experimental and numerical identification of flutter derivatives for nine bridge deck sections", *Wind Struct.*, **12**(6), 519-540.

Sumer, B.M. and Fredsøe, J. (1997), "Hydrodynamics Around Cylindrical Structures", *Adv. Ser. Ocean Eng*.

Tang, H., Li, Y., Wang, Y. and Tao, Q. (2017), "Aerodynamic optimization for flutter performance of steel truss stiffening girder at large angles of attack", *J. Fluid Struct.*, **168**, 260-270.

Wu, T. and Kareem, A. (2013), "Aerodynamics and aeroelasticity of cable-supported bridges: Identification of nonlinear features", *J. Eng. Mech.*, **139**(12), 1886-1893.

Wu, T. and Kareem, A. (2013a), "A nonlinear convolution scheme to simulate bridge aerodynamics", *Comput. Struct.*, **128**, 259-271.

Wu, T. and Kareem, A. (2013b), "Bridge aerodynamics and aeroelasticity: A comparison of modeling schemes", *J. Fluid Struct.*, **43**, 347-370.

Wu, T. and Kareem, A. (2015), "A nonlinear analysis framework for bluff-body aerodynamics: A Volterra representation of the solution of Navier-Stokes equations", *J. Fluid Struct.*, **54**, 479-502.

FR